Band structure and end states in InAs/GaSb core-shell-shell nanowires

Florinda Viñas Boström⊙, Athanasios Tsintzis, Michael Hell, and Martin Leijnse

Division of Solid State Physics and NanoLund, Lund University, Box 118, S-221 00 Lund, Sweden

Quantum wells in InAs/GaSb heterostructures can be tuned to a topological regime associated with the quantum spin Hall effect, which arises due to an inverted band gap and hybridized electron and hole states. Here, we investigate electron-hole hybridization and the fate of the quantum spin Hall effect in a quasi-one-dimensional geometry, realized in a core-shell-shell nanowire with an insulator core and InAs and GaSb shells. We calculate the band structure for an infinitely long nanowire using $\mathbf{k} \cdot \mathbf{p}$ theory within the Kane model and the envelope function approximation, then map the result onto a Bernevig-Hughes-Zhang model which is used to investigate finite-length wires. Clearly, quantum spin Hall edge states cannot appear in the core-shell-shell nanowires which lack one-dimensional edges, but in the inverted band gap regime we find that the finite-length wires instead host localized states at the wire ends. These end states are not topologically protected; they are fourfold degenerate and split into two Kramers pairs in the presence of potential disorder along the axial direction. However, there is some remnant of the topological protection of the quantum spin Hall edge states in the sense that the end states are fully robust to (time-reversal preserving) angular disorder, as long as the bulk band gap is not closed.

I. INTRODUCTION

The InAs/GaSb material system has attracted interest due to its broken band gap alignment [see Fig. 1(a)], with large overlap of conduction bands (CBs) and valence bands (VBs), leading to hybridized electron-hole states in low-dimensional systems. The system has previously been studied in quantum wells (QWs) [1–3], often sandwiched between AlSb barriers [see Fig. 1(b)]. Compared to the broken band gap alignment in bulk (an interface between two semi-infinite material layers), confinement in the QW moves the CBs up and the VBs down, which can restore a band gap. However, if confinement is not large enough to give a conventional band gap, hybridization of the CBs and VBs can still cause an effective band gap to open up. We define such a hybridization gap as a band gap where the VB band edge lies above the CB band edge. InAs/GaSb QWs are known for exhibiting the quantum spin Hall effect in this inverted regime [1,2] and hence are topological insulators [4]. The topological insulators host edge states which are spin and momentum locked, carrying spin currents in two opposite directions. These states are robust to perturbations as long as time reversal symmetry is not broken.

In addition to the QWs, InAs/GaSb core-shell nanowires (NWs) have been investigated both experimentally and theoretically [5–15]. Core-shell NWs with one shell are grown by several groups today [8–16], and NWs with two shells can be grown [16], e.g., with the aim of passivating the outer InAs layer [14].

In this work we study cylindrical core-shell-shell NWs, where an insulator core is radially overgrown with one InAs layer and one GaSb layer [see Fig. 1(c)]. This system is in class AII, which lacks a topological phase in one dimension (1D) [17]. However, a core-shell-shell NW, as depicted in Fig. 1(c), is not strictly 1D [and in the limit of an infinite radius it tends to a two-dimensional (2D) QW system]. Using the $\mathbf{k} \cdot \mathbf{p}$ Kane model, we show that the hybridization gap seen in the QW persists in the NW we consider for suitable InAs and GaSb shell thicknesses. Using a Bernevig-Hughes-Zhang (BHZ) model [18] with parameters taken from fitting to the $\mathbf{k} \cdot \mathbf{p}$ band structures, we study a finite NW and conclude that the core-shell-shell NWs can host end states. However, even though these end states originate from the QW edge states, they are different since the edge states gap out when we "roll up" the QWs. The NW end states are not robust to axial disorder, in contrast to the topologically protected edge modes in QWs. However, the end states are robust to (time-reversal preserving) disorder in the angular direction of the NW.

This paper is organized as follows: in Sec. II we present the Kane model, the BHZ model, and the discretization scheme we use to calculate the spectra and the wave functions of the NW and QW systems. In Sec. III we present the results together with a discussion. Section IV contains a brief conclusion.

II. METHOD

We use a Kane model [19] to obtain the band structures of the QWs and the NWs. The Kane Hamiltonian is given by [19–21]

$$H = \begin{pmatrix} H_{4\times4} & 0 \\ 0 & H_{4\times4} \end{pmatrix} + H_{\mathrm{SOC}}, \qquad (1)$$

with

$$H_{4\times4} = \varepsilon_v(\mathbf{k})\begin{pmatrix} 0 & 0 \\ 0 & \mathbb{1}_{3\times3} \end{pmatrix}$$

$$+ \begin{pmatrix} H_{CC} & iPk_x & iPk_y & iPk_z \\ \dagger & k_xLk_x + k_yMk_y + k_zMk_z & k_x\frac{N}{2}k_y + k_y\frac{N}{2}k_x & k_x\frac{N}{2}k_z + k_z\frac{N}{2}k_x \\ \dagger & \dagger & k_xMk_x + k_yLk_y + k_zMk_z & k_y\frac{N}{2}k_z + k_z\frac{N}{2}k_y \\ \dagger & \dagger & \dagger & k_xMk_x + k_yMk_y + k_zLk_z \end{pmatrix}, \qquad (2)$$

with

$$H_{CC} = E_c + k_xAk_x + k_yAk_y + k_zAk_z, \qquad (3)$$

$$\varepsilon_v(\mathbf{k}) = E_v - \frac{\Delta_{\text{SOC}}}{3} + \frac{\hbar^2}{2m_0}\mathbf{k}^2, \qquad (4)$$

and

$$H_{\text{SOC}} = \frac{\Delta_{\text{SOC}}}{3}\begin{pmatrix} 0 & 0 & 0 & 0 & 0 & 0 & 0 & 0 \\ 0 & 0 & -i & 0 & 0 & 0 & 0 & 1 \\ 0 & i & 0 & 0 & 0 & 0 & 0 & -i \\ 0 & 0 & 0 & 0 & 0 & -1 & i & 0 \\ 0 & 0 & 0 & 0 & 0 & 0 & 0 & 0 \\ 0 & 0 & 0 & -1 & 0 & 0 & i & 0 \\ 0 & 0 & 0 & -i & 0 & -i & 0 & 0 \\ 0 & 1 & i & 0 & 0 & 0 & 0 & 0 \end{pmatrix}. \qquad (5)$$

Here, E_c is the bottom of the CB and E_v the top of the VB, so that the bulk band gap is $E_g = E_c - E_v$. The Hamiltonian is written in the CB-VB and spin basis,

$$\{|S\uparrow\rangle, |P_X\uparrow\rangle, |P_Y\uparrow\rangle, |P_Z\uparrow\rangle,$$
$$|S\downarrow\rangle, |P_X\downarrow\rangle, |P_Y\downarrow\rangle, |P_Z\downarrow\rangle\}, \qquad (6)$$

where the CB states $\{|S\rangle\}$ are given by s orbitals and the VB states $\{|P\rangle\}$ are given by p orbitals. The parameters used in the Kane Hamiltonian are given in terms of Luttinger parameters and the electron vacuum mass m_0 as

$$P = \sqrt{\frac{\hbar^2}{2m_0}E_P},$$

$$L = -\frac{\hbar^2}{2m_0}(\gamma_1 + 4\gamma_2) + \frac{P^2}{E_g},$$

$$M = -\frac{\hbar^2}{2m_0}(\gamma_1 - 2\gamma_2),$$

$$N = -6\frac{\hbar^2}{2m_0}\gamma_3 + \frac{P^2}{E_g},$$

$$A = \frac{\hbar^2}{2m_0}. \qquad (7)$$

To be able to compare to works on InAs/GaSb QWs, we use the parameters from Ref. [22], in accordance with Refs. [23,24]. The parameter values are given in Table I. We consider the QWs and the NWs to be grown in the [111] direction. To obtain the Kane Hamiltonian in this crystallographic direction, we must impose a rotation of the coordinate system of the Hamiltonian [25]. This process is discussed in

Ref. [5] and follows Refs. [25–27]. The NWs are modeled to be cylindrical, but we point out that the difference in electronic structure compared with NWs with hexagonal cross sections is expected to be small, especially for the relatively large radii we consider [27]. We solve the Schrödinger equation for the Kane Hamiltonian within the envelope function approximation to include the effect of the different materials and geometries. The envelope function approximation is employed by substituting $k_n \rightarrow -i\partial_n$ in Eq. (1) for the directions n where translational symmetry is broken. We then use a basis function expansion of the envelope functions ψ. In the calculations for the QW, a plane wave basis is used in the growth direction z. In the calculations for the NWs, assumed to be cylindrical, we assume plane waves in the growth direction z and expand ψ in a basis consisting of approximations to the Bessel functions far from the origin in the radial direction [28] r,

$$f_{m,n}(r, \theta) = \eta(m, n)\frac{1}{\sqrt{r}}\sin\left(\frac{R - r}{R_c - R}m\pi\right)e^{in\theta}, \qquad (8)$$

where $\eta(m, n)$ is a normalization factor. In the calculations the basis expansions are truncated after convergence is reached.

For computational reasons, we consider the core-shell-shell NW to be hollow, in the sense that the inner core consists of vacuum, as in Fig. 1(c). However, in a real experimental structure the full core could be filled with AlSb without affecting the energy dispersion for the states around the gap. One can also imagine another insulator core (or possibly vacuum) instead of this filled AlSb core. In this case, we expect that the results will not change qualitatively because, as we will see, the wave functions around the gap penetrate very little into the AlSb layer. In the NW system we use one inner AlSb barrier, as in Fig. 1(c), while for the QW calculations we use AlSb barriers on both sides of the structure [see Fig. 1(b)]. We choose these configurations because this is how the structures would most likely be grown. In addition, these configurations

TABLE I. The parameters used in the Kane model. The VB offsets between the materials are given by $E_{\text{GaSb/InAs}} = 0.56$ eV and $E_{\text{AlSb/InAs}} = 0.18$ eV.

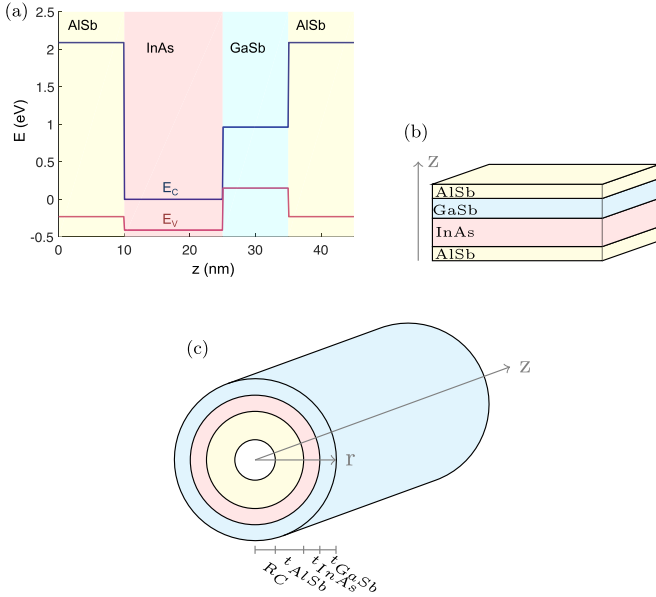|	InAs	GaSb	AlSb
E_g (eV)	0.41	0.8128	2.32
E_P (eV)	22.2	22.4	18.7
γ_1	19.67	11.80	4.15
γ_2	8.37	4.03	1.01
γ_3	9.29	5.26	1.75
Δ_{SOC} (eV)	0.38	0.752	0.75

FIG. 1. (a) Band diagram for the InAs/GaSb/AlSb material system. Sketches showing (b) the quantum well structure and (c) the core-shell-shell nanowire we consider.

FIG. 2. (a) Band structure for a QW calculated using $\mathbf{k} \cdot \mathbf{p}$ theory with $t_{AlSb} = 10$ nm, $t_{InAs} = 11$ nm, and $t_{GaSb} = 5$ nm for $k_x = 0$. (b) Band structure reproduced with the BHZ Hamiltonian for an infinite QW system for $k_x = 0$. The parameters used are given in Table II.

avoid problems with spurious solutions (a removal of the AlSb barriers causes the wave functions to oscillate in a nonphysical way). The spurious solutions are unphysical solutions to the Schrödinger equation for the Kane Hamiltonian that can arise when employing the envelope function approximation [20,21,25,29].

We use a BHZ model as a complement to the $\mathbf{k} \cdot \mathbf{p}$ calculations in order to study end states of a finite NW and to add disorder to the system. The reason that we use this model to study a finite system is that it becomes too numerically expensive to solve using our $\mathbf{k} \cdot \mathbf{p}$ model. The BHZ model [1,18,30] is given by

$$H = H_{\text{BHZ}} + H_{\text{SIA}}, \quad (9)$$

where

$$H_{\text{BHZ}} = \begin{pmatrix} h(k) & 0 \\ 0 & h^*(-k) \end{pmatrix}, \quad (10)$$

with

$$h(k) = \begin{pmatrix} \epsilon(k) + M(k) & Ak_+ \\ Ak_- & \epsilon(k) - M(k) \end{pmatrix} \quad (11)$$

and $\epsilon(k) = C - D(k_x^2 + k_y^2)$, $M(k) = M - B(k_x^2 + k_y^2)$, $k_\pm = k_x \pm ik_y$. H_{BHZ} is written in the basis $(|CB+\rangle, |VB+\rangle, |CB-\rangle, |VB-\rangle)^T$. $|CB\pm\rangle$ ($|VB\pm\rangle$) corresponds to the lowest (highest) energy subband originating from the CB (VB) in InAs (GaSb), and $\pm$ denotes Kramers partners. Structural inversion asymmetry (SIA) spin splitting, which is intrinsic in the $\mathbf{k} \cdot \mathbf{p}$ model, is explicitly included here [1]:

$$H_{\text{SIA}} = \begin{pmatrix} 0 & 0 & -iR_0k_- & 0 \\ 0 & 0 & 0 & iT_0k_-^3 \\ iR_0k_+ & 0 & 0 & 0 \\ 0 & -iT_0k_+^3 & 0 & 0 \end{pmatrix}. \quad (12)$$
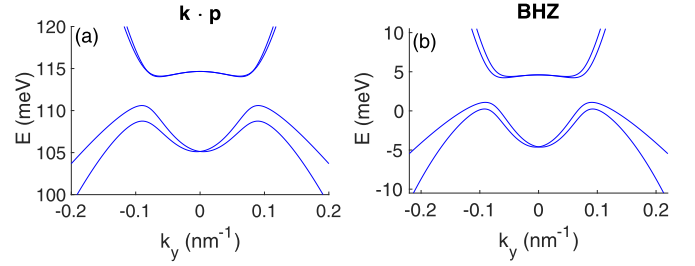
Along with the linear-k (R_0) term coupling CB-like states, a cubic-k (T_0) term coupling VB-like states has also been included, following Ref. [30]. A second-order SIA term coupling CB-like and VB-like states is also generally present, but it has very little effect on the band structures we wish to reproduce and is therefore omitted. We do not consider bulk inversion asymmetry terms, as they are negligible for InAs/GaSb QWs [31].

The Hamiltonian in Eq. (9) can be readily used to reproduce the $\mathbf{k} \cdot \mathbf{p}$ band structure in the infinite QW system. The finite QW can be studied by discretizing Eq. (9) on a square lattice of finite dimensions and is found to host midgap Kramers-degenerate topological edge states for a wide parameter range [1]. Considering the 2D QW in the y-z plane instead and with periodic boundary conditions along the y direction, the system is in a "rolled-up" geometry equivalent to a cylindrical NW with the growth axis along z.

III. RESULTS

Figure 2(a) shows the band structure for a QW with $t_{InAs} = 11$ nm and $t_{GaSb} = 5$ nm, calculated using $\mathbf{k} \cdot \mathbf{p}$ theory. The corresponding band structure from BHZ calculations is shown in Fig. 2(b). The parameters (see Table II) for the BHZ model are chosen to give a good match with the $\mathbf{k} \cdot \mathbf{p}$ band structure. The band structures are in good agreement with previous works [23] and show a hybridization gap. For an ordinary confinement gap to open up, the gap needs to close and reopen. The QW is known to host topologically protected edge states in this inverted regime.

We now shift our attention to the main subject of our study, namely, InAs/GaSb core-shell-shell NWs. Figure 3(a) shows

TABLE II. BHZ parameters used in Fig. 2(b). The rest of the parameters appearing in Eqs. (9)–(12) are set to zero.

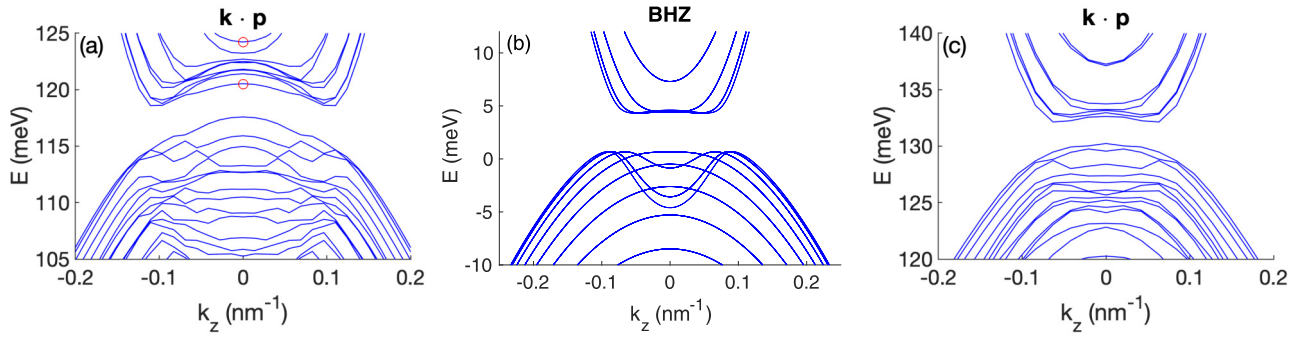| Parameter	Value
A (meV nm)	30.5
B (meV nm^2)	-710
D (meV nm^2)	-450
M (meV)	-4.6
R_0 (meV nm)	10
T_0 (meV nm^3)	300

FIG. 3. (a) Band structures calculated using the $\mathbf{k} \cdot \mathbf{p}$ model with $R_c = 10$ nm, $t_{AlSb} = 14$ nm, $t_{InAs} = 11$ nm, and $t_{GaSb} = 5$ nm. (b) Band structure calculated using the discretized BHZ model with $R_{BHZ} = 32$ nm and no SIA terms included ($R_0 = T_0 = 0$). The rest of the parameters are the same as in Fig. 2(b). (c) Same as (a), but with $t_{InAs} = 9.5$ nm and $t_{GaSb} = 6.5$ nm.

the band structure for such a core-shell-shell NW, calculated using the Kane model, with $t_{InAs} = 11$ nm, $t_{GaSb} = 5$ nm, $R_C = 10$ nm, and $t_{AlSb} = 14$ nm, so the thicknesses of InAs and GaSb are the same as in Fig. 2(a). The band gap is only $E_g = 1$ meV, compared to the larger value of $E_g = 3.4$ meV for the QW (for the same thicknesses of InAs and GaSb). The main reason for this smaller gap is that the confinement effects are different in the NW system and possibly that in the core-shell-shell NW the curvature effects also become important. The angular subbands are much closer in energy than the radial ones, which makes sense if we compare the length scales: the radial confinement is roughly $t_{InAs} + t_{GaSb} = 16$ nm, while confinement in the angular direction is of the magnitude $2\pi R \approx 250$ nm. All subbands are twofold degenerate because both time reversal and structural inversion symmetries are present.

In Fig. 3(b) we show a band structure calculated with the discretized BHZ model, using the same parameters as in Fig. 2(b), but with periodic boundary conditions along one direction. To reflect the symmetries of the cylindrical NW geometry, we set the SIA terms to zero ($R_0 = 0$, $T_0 = 0$). We choose the value of the radius ($R_{BHZ} = 32$ nm) to be in between the inner and outer radii in the $\mathbf{k} \cdot \mathbf{p}$ calculations. We believe that the main reason that the band structures in Figs. 3(a) and 3(b) look so different is that the confinement effects in the $\mathbf{k} \cdot \mathbf{p}$ calculations become very different in a cylindrical geometry.

Figure 3(c) shows that we can obtain a band structure from $\mathbf{k} \cdot \mathbf{p}$ calculations that is similar to the one in Fig. 3(b) by changing the shell thicknesses of the InAs and GaSb shells to $t_{InAs} = 9.5$ nm and $t_{GaSb} = 6.5$ nm. The core radius and the AlSb shell thickness are $R_C = 10$ nm and $t_{AlSb} = 14$ nm, the same as in Fig. 3(a). We note that the hybridization gap is $E_g^{k \cdot p} = 1.9$ meV, smaller than the hybridization gap $E_g^{BHZ} = 3.7$ meV from the BHZ results.

Figure 4 shows the probability density in the radial direction $\rho_j(r) = r|\Psi_{j,k_z=0}(r)|^2 = \sum_{i=1}^{8} |\psi_{i,j,k_z=0}(r)|^2$ for two different subbands j in Fig. 3(a), calculated using the Kane model. The probability density for the lowest-lying subband above the gap is plotted in blue and shows a state mostly confined in the outer shell. The red line shows the probability density for the topmost subband seen in Fig. 3(a). Even though this subband looks like a pure CB state for small k_z, we see

that the state has large weight in both the InAs and GaSb shells. In general, most of the subbands around the band gap have weight in both these outer shells or predominantly in the GaSb shell. To find states confined in the InAs shell, one has to study subbands much higher ($\sim$50 meV) above the gap.

Next, we use the BHZ model with the fitted parameters to study the fate of the QW's edge states in the NW geometry. This is meant in the sense that one can imagine arriving at a finite NW geometry by rolling up a finite 2D QW system. Coupling two of the edges causes the edge states to gap out. However, we find that this leaves localized end states at both NW ends. Figure 5(a) shows the energies of the end states together with the more closely spaced bulk states using the same parameters as in Fig. 3(b), but the system is now taken to be finite in z ($L_{NW} = 1000$ nm). One major difference between the end states seen for the NW system compared to the edge states in the QW is that the NW end states are doubly degenerate *in each Kramers sector* (fourfold degenerate in total), while for the QW the edge states are only Kramers degenerate. In Fig. 5(b) the probability density along the NW for the zero angular momentum end state is plotted. For the chosen NW length the weights of the wave functions in this fourfold-degenerate subspace are highly localized at the NW ends.

The robustness of the end states can be checked by including disorder effects in the NW discretized BHZ model.
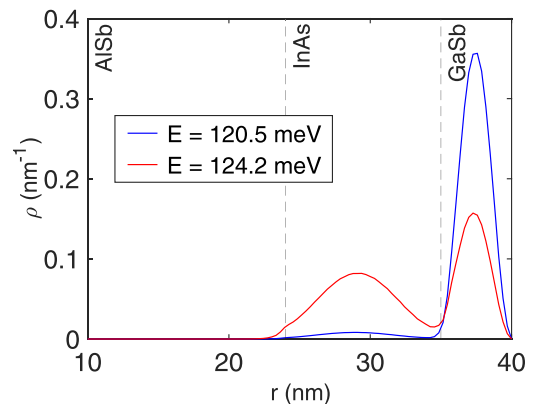

FIG. 4. Probability density $\rho(r)$ for the two subbands marked with red in Fig. 3(a) for $k_z = 0$: the first subband above the gap (blue line) and the topmost subband seen in Fig. 3(a) (red line).
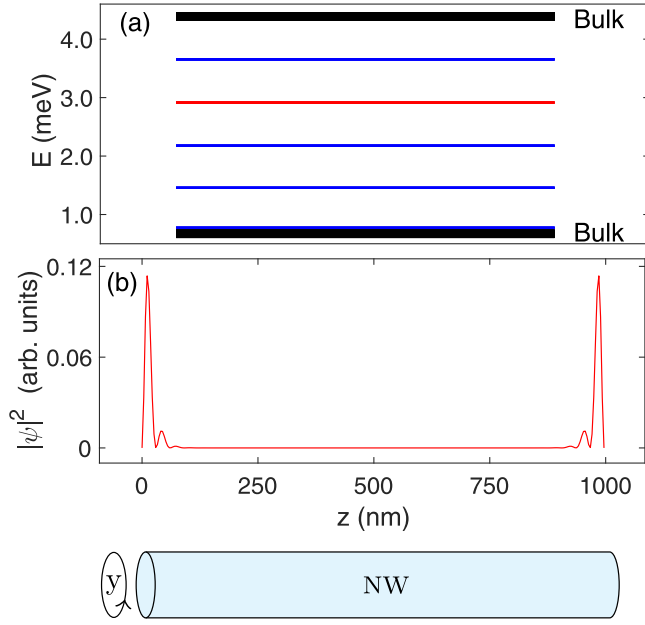
FIG. 5. (a) End and bulk state energies for a NW of length $L_{NW} = 1000$ nm obtained from BHZ calculations. The zero angular momentum end state is colored red, and the higher angular momentum end states are blue, while the bulk states are black. The rest of the parameters are the same as in Fig. 3(b). (b) Probability density of the zero angular momentum wave function along the NW growth axis.
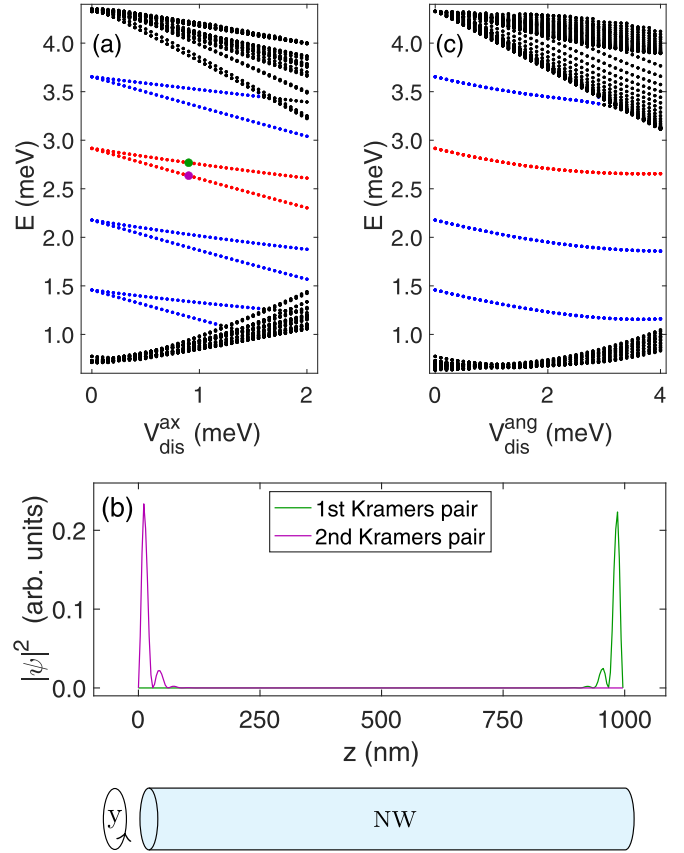

FIG. 6. (a) Evolution of the finite system eigenvalues with increasing axial disorder obtained from the discretized BHZ model. The color code is the same as in Fig. 5(a). The states stemming from the splitting of the zero angular momentum end state are marked with the green and magenta dots. (b) Probability density for the marked states along the NW growth axis. (c) Evolution of the finite system eigenvalues with increasing angular disorder. Apart from disorder, the parameters are the same as in Fig. 5(a).

First, we consider disorder in the axial (growth) direction (V_{dis}^{ax}) and no disorder in the angular direction. For each set of sites with the same axial coordinate z, identical disorder terms $H_{dis}^{ax}(z) = a(z)V_{dis}^{ax}\mathbb{1}_{4\times4}$ are added to the corresponding 4×4 on-site submatrices of the discretized version of Eq. (9), where each $a(z)$ is a random number from a uniform distribution in the interval $[-1, 1]$. For n sites in the z direction, n random $a(z) \equiv a(nd) = a_n$ are chosen ($d = 5$ nm is the lattice constant). The same set of a_n's is used for the different disorder strengths V_{dis}^{ax}. In Fig. 6(a) we show the evolution of the eigenvalues of Fig. 5(a) with increasing disorder strength for a typical set of a_n's (corresponding to a single typical disorder realization). The color code is the same as in Fig. 5(a). The most striking effect is the splitting of the end states' energies with increasing disorder. Since the disorder is time reversal symmetry preserving, each eigenvalue remains Kramers degenerate also for $V_{dis}^{ax} \neq 0$. The Kramers-degenerate eigenvalues stemming from the splitting of the zero angular momentum end state energy for a disorder strength of $V_{dis}^{ax} = 0.9$ meV are marked with green and magenta dots. The wave functions' amplitudes squared along the NW axis corresponding to the marked states are plotted in Fig. 6(b). The states remain localized at the ends of the wire for $V_{dis}^{ax} \neq 0$, and their energy splitting cannot be attributed to wave functions overlapping due to the finite wire length. The splitting is a signature of the lack of topological protection of the end states.

Despite the above general conclusion, it turns out that some aspects of topological protection remain for the end states of the NW. This becomes evident if one considers a different type of disorder. Figure 6(c) also shows the evolution of the

eigenvalues of Fig. 5(b) with increasing disorder strength, but this time the disorder is in the angular direction (V_{dis}^{ang}), and $V_{dis}^{ax} = 0$. The discretized Hamiltonian is obtained with a procedure similar to the axial disorder case, but here, the disorder terms $H_{dis}^{ang}(y) = b(y)V_{dis}^{ang}\mathbb{1}_{4\times4}$ are added to sites with the same angular coordinate y. The end states do not split in this case, and they remain fourfold degenerate, undisturbed by disorder.

IV. CONCLUSIONS

We have studied InAs/GaSb core-shell-shell NWs by calculating their electronic band structure and wave functions. We find that, as in the case for QWs of the same materials, a hybridization gap can exist and that the system hosts in-gap end states in this inverted regime. The end states could be probed experimentally by, for example, tunnel spectroscopy. The end states are twofold degenerate within each Kramers sector and gap out when subjected to axial disorder. However, disorder in the radial direction leaves the end states unaffected, as long as the bulk gap persists.

ACKNOWLEDGMENTS

[1] C. Liu, T. L. Hughes, X. L. Qi, K. Wang, and S. C. Zhang, Phys. Rev. Lett. **100**, 236601 (2008).

[2] I. Knez, R. R. Du, and G. Sullivan, Phys. Rev. Lett. **107**, 136603 (2011).

[3] F. Nichele, H. J. Suominen, M. Kjaergaard, C. M. Marcus, E. Sajadi, J. A. Folk, F. Qu, A. J. A. Beukman, F. K. de Vries, J. van Veen, S. Nadj-Perge, L. P. Kouwenhoven, B.-M. Nguyen, A. A. Kiselev, W. Yi, M. Sokolich, M. J. Manfra, E. M. Spanton, and K. A. Moler, New J. Phys. **18**, 083005 (2016).

[4] M. Z. Hasan and C. L. Kane, Rev. Mod. Phys. **82**, 3045 (2010).

[5] F. Viñas, H. Q. Xu, and M. Leijnse, Phys. Rev. B **95**, 115420 (2017).

[6] V. V. Ravi Kishore, B. Partoens, and F. M. Peeters, Phys. Rev. B **86**, 165439 (2012).

[7] N. Luo, G.-Y. Huang, G. Liao, L.-H. Ye, and H. Q. Xu, Sci. Rep. **6**, 38698 (2016).

[8] M. Ek, B. M. Borg, A. W. Dey, B. Ganjipour, C. Thelander, L. E. Wernersson, and K. A. Dick, Cryst. Growth Des. **11**, 4588 (2011).

[9] B. Ganjipour, M. Ek, B. Mattias Borg, K. A. Dick, M.-E. Pistol, L.-E. Wernersson, and C. Thelander, Appl. Phys. Lett. **101**, 103501 (2012).

[10] B. Ganjipour, M. Leijnse, L. Samuelson, H. Q. Xu, and C. Thelander, Phys. Rev. B **91**, 161301(R) (2015).

[11] J. G. Gluschke, M. Leijnse, B. Ganjipour, K. A. Dick, H. Linke, and C. Thelander, ACS Nano **9**, 7033 (2015).

[12] T. Rieger, D. Grützmacher, and M. I. Lepsa, Nanoscale **7**, 356 (2015).

[13] L. Namazi, M. Nilsson, S. Lehmann, C. Thelander, and K. A. Dick, Nanoscale **7**, 10472 (2015).

[14] M. Nilsson, L. Namazi, S. Lehmann, M. Leijnse, K. A. Dick, and C. Thelander, Phys. Rev. B **94**, 115313 (2016).

[15] M. Rocci, F. Rossella, U. P. Gomes, V. Zannier, F. Rossi, D. Ercolani, L. Sorba, F. Beltram, and S. Roddaro, Nano Lett. **16**, 7950 (2016).

[16] L. J. Lauhon, M. S. Gudiksen, D. Wang, and C. M. Lieber, Nature (London) **420**, 57 (2002).

[17] A. Altland and M. R. Zirnbauer, Phys. Rev. B **55**, 1142 (1997).

[18] B. A. Bernevig, T. L. Hughes, and S.-C. Zhang, Science **314**, 1757 (2006).

[19] E. O. Kane, J. Phys. Chem. Solids **1**, 249 (1957).

[20] B. A. Foreman, Phys. Rev. B **56**, R12748(R) (1997).

[21] S. Birner, Ph.D. thesis, Technische Universität München, 2011.

[22] E. Halvorsen, Y. Galperin, and K. A. Chao, Phys. Rev. B **61**, 16743 (2000).

[23] A. Zakharova, S. T. Yen, and K. A. Chao, Phys. Rev. B **64**, 235332 (2001).

[24] F. Nichele, M. Kjaergaard, H. J. Suominen, R. Skolasinski, M. Wimmer, B.-M. Nguyen, A. A. Kiselev, W. Yi, M. Sokolich, M. J. Manfra, F. Qu, A. J. A. Beukman, L. P. Kouwenhoven, and C. M. Marcus, Phys. Rev. Lett. **118**, 016801 (2017).

[25] M. Willatzen and L. C. Lew Yan Voon, *The kp Method* (Springer, Berlin, 2009).

[26] B. Lassen, M. Willatzen, R. Melnik, and L. C. Lew Yan Voon, J. Mater. Res. **21**, 2927 (2006).

[27] N. Luo, G. Liao, and H. Q. Xu, AIP Adv. **6**, 125109 (2016).

[28] M. Abramowitz, *Handbook of Mathematical Functions, with Formulas, Graphs, and Mathematical Tables* (Dover Publications, New York, 1974).

[29] R. Winkler, *Spin Orbit Coupling Effects in Two-Dimensional Electron and Hole Systems* (Springer, New York, 2003).

[30] D. G. Rothe, R. W. Reinthaler, C. X. Liu, L. W. Molenkamp, S. C. Zhang, and E. M. Hankiewicz, New J. Phys. **12**, 065012 (2010).

[31] C. Liu and S. Zhang, in *Topological Insulators*, edited by M. Franz and L. Molenkamp, Contemporary Concepts of Condensed Matter Science Vol. 6 (Elsevier, Oxford, 2013).